Near-field imaging with a loaded wire medium

Chandra S. R. Kaipa,[1,*] Alexander B. Yakovlev,[1] Stanislav I. Maslovski,[2] and Mário G. Silveirinha[2]
[1]*Department of Electrical Engineering, The University of Mississippi, University, Mississippi 38677, USA*
[2]*Department of Electrical Engineering-Instituto de Telecomunicações, University of Coimbra, 3030 Coimbra, Portugal*
(Received 25 June 2012; revised manuscript received 4 September 2012; published 1 October 2012)

It is shown that a bi-layer mushroom structure formed by two coupled metallic grids may enable the resonant enhancement of the near field and superlensing at microwave and terahertz frequencies, to some extent analogous to the silver lens at UV. The charge density waves supported by the two grids can be strongly coupled, even if the thickness of the bi-layer mushroom is a significantly large fraction of the wavelength. The imaging properties can be controlled by changing the structural parameters of the bi-layer mushroom.

DOI: 10.1103/PhysRevB.86.155103 PACS number(s): 78.20.Ci, 42.70.Qs, 41.20.Jb, 78.66.Sq

I. INTRODUCTION

Since the introduction of the concept of the perfect lens,[1] there has been a great interest in the theoretical investigation and practical realization of metamaterial-based lenses that can restore both the propagating waves (focusing of rays based on negative refraction as theoretically suggested by V. G. Veselago) and the evanescent waves (targeting the recovery of the fine spatial features by resonant effects) of a source at the image plane. These lenses, also known as superlenses, may surpass the performance of conventional diffraction limited lenses, and may have important applications in biomedical imaging, sensing, nondestructive characterization of materials, microwave heating, and many other technological areas.[2–9]

It is well known that the evanescent wave amplification in Pendry's lens is due to the resonant excitation of a pair of coupled surface-wave modes (plasmon and antiplasmon) at the slab interfaces.[10,11] Based on this property, it was shown that a bulk material is not required to achieve this phenomenon, and that it can be realized simply by using a pair of resonant grids or conjugate sheets separated by a suitable distance.[12–15] Also, imaging with subwavelength resolution can be achieved without materials with negative effective parameters.[7,16,17]

Here, we demonstrate the possibility of near-field imaging based on mushroom-type metamaterials, as a continuation of our previous work on the analysis of reflection/transmission properties, natural modes, and negative refraction in these structures.[18–20] The main motivation is that the previous studies[19,21,22] have shown that mushroom-type substrates can support strongly confined guided modes that to some extent mimic the role of surface plasmon polaritons at optics. Similar to conventional plasmons, these strongly localized waves—which are sometimes designated by "spoof plasmons"[22–24]—are rooted in the resonant interaction of the electromagnetic field and the charge density oscillations in metals. However, while in bulk metals, the characteristic spatial period of oscillations of the electron gas is directly determined by the electron mass and by the electron concentration, in the case of spoof plasmons the oscillations of the charge density are determined by the characteristic size of the metallic patterns obtained by structuring a bulk metal. Due to this reason, the frequency of resonance of spoof plasmons can be several orders of magnitude smaller than the resonance frequency of plasmon polaritons in bulk metals.

Based on these ideas, we investigate near-field enhancement by a bi-layer mushroom structure with inductive/capacitive loadings. The bi-layer mushroom structure consists of two metallic grids connected by loaded metallic wires. The role of impedance loadings (lumped impedance insertions) is to provide a controllable coupling between the charge density waves supported by each grid, which is the key to achieve subwavelength imaging in the considered structure. This mechanism is to some extent analogous to that of the silver lens.[1,27] However, we prove that due to the unusual waveguiding and channeling properties of the wire medium, the two grids can be strongly coupled even if they are separated by a significant distance. In particular, our system enables a superlensing effect even if the distance between the two grids is a significant fraction of the wavelength, which contrasts with the silver lens whose optimal thickness is equal to the distance that the wave propagates in free-space.[1] It should be noted that a uniaxial wire medium (WM) has been used previously to achieve sub-diffraction imaging.[25] However, the imaging mechanism in Ref. 25 was based on the conversion of evanescent waves into transmission-line modes (based on the principle of canalization), and it does not involve the enhancement of evanescent waves.[26]

Our analysis is carried out using the homogenization models for uniaxial WM with impedance loadings.[18,20] The predictions of the homogenization results are validated against the full-wave numerical results obtained with a finite-element program HFSS.[32]

The paper is organized as follows. In Sec. II, we give the closed-form expressions for the reflection/transmission coefficients of the loaded WM slab based on an effective medium model. In Sec. III, the dispersion behavior of the guided modes of the bi-layer mushroom structure is investigated. Sections IV and V describe the designs of mushroom structures with inductive/capacitive loadings, demonstrating a significant amplification of the evanescent waves and a superlensing effect. The conclusions are drawn in Sec. VI. A time dependence of the form of $e^{j\omega t}$ is assumed and suppressed.

II. ANALYTICAL MODEL FOR THE BI-LAYER MUSHROOM STRUCTURE

The geometry of the bi-layer mushroom structure is represented in Fig. 1. It consists of two metallic grids formed

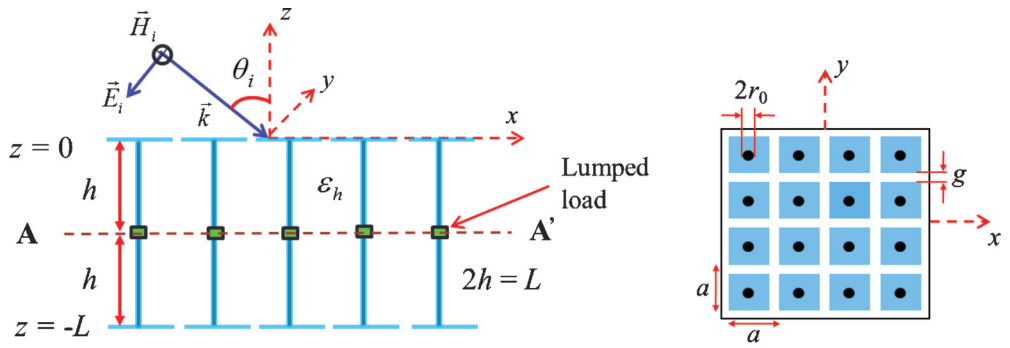

(a) (b)

FIG. 1. (Color online) Geometry of the bi-layer mushroom structure with the lumped loads at the center of the metallic wires, illuminated by an obliquely incident TM-polarized plane wave. (a) Cross-section view and (b) top view.

by square patches arranged in a square lattice with period a. The lateral gap between the patches is g. The two grids are separated by a dielectric with permittivity ε_h, and are connected by wires with radius r_0, oriented along the z direction. We allow for the presence of discrete impedance insertions (lumped loads) at the center of the wires at the plane $z = -h$, with $h = L/2$. These lumped elements provide increased degrees of freedom in the design, and their role is discussed in details ahead.

Following our previous studies,[18,20] the electromagnetic response of the bi-layer mushroom structure can be described using an effective medium approach. In our model, the two grids are treated as impedance sheets, whereas the WM slab is modeled as a uniaxial continuous material characterized by a nonlocal effective dielectric function[28] along the direction of the wires such that $\varepsilon_{zz} = \varepsilon_h[1 - k_p^2/(k_h^2 - k_z^2)]$, where $k_h = k_0\sqrt{\varepsilon_h}$ is the wave number in the host medium, $k_0 = \omega/c$ is the free-space wave number, k_z is the z component of the wave vector $\vec{k} = (k_x,0,k_z)$ inside the material, and following Ref. 29 the plasma wave number is taken equal to $k_p = \sqrt{(2\pi/a^2)/\ln[a^2/4r_0(a - r_0)]}$.

To determine the response of the structured slab under the transverse magnetic (TM) plane-wave excitation, we can exploit the symmetry of the structure with respect to the AA' plane at $z = -h$ (see Fig. 1). For odd and even excitations of the incident magnetic field H_y, the symmetry plane AA' corresponds to a perfect magnetic conductor (PMC) and a perfect electric conductor (PEC), respectively. In the PEC case, only half of the value of the load impedance needs to be considered at the connection to the PEC ground plane (such that the inductive/capacitive load of the entire structure in Fig. 1 is obtained by the series connection). In the PMC case, the current at the connection between the wires and the equivalent PMC plane vanishes, and thus the lumped load plays no role.

The analytical expression of the reflection coefficient for the even excitation (PEC symmetry) was derived in Ref. 19,

$$R_{\text{even}} = \frac{(jk_0 - \eta_0\gamma_0 Y_g)K - jk_0\gamma_0 M}{(jk_0 + \eta_0\gamma_0 Y_g)K + jk_0\gamma_0 M}, \tag{1}$$

where η_0 is the intrinsic impedance of free space, $\gamma_0 = \sqrt{k_x^2 - k_0^2}$ is the propagation constant in free space, and $k_x = k_0 \sin\theta_i$ is the x component of the wave vector $\vec{k}$. In Eq. (1), $Y_g = j(\varepsilon_h + 1)(k_0 a/\eta_0\pi)\ln[\csc(\pi g/2a)]$ is the grid admittance of the patch array,[31]

$$K = \gamma_{\text{TM}}\sinh(\gamma_{\text{TM}}h)\cos(k_{\text{TEM}}h) - k_{\text{TEM}}\sin(k_{\text{TEM}}h) \times \left[\left(\frac{\varepsilon_h}{\varepsilon_{zz}^{\text{TM}}} - 1\right)\cosh(\gamma_{\text{TM}}h) + \frac{\varepsilon_h\gamma_{\text{TM}}\sinh(\gamma_{\text{TM}}h)}{\varepsilon_{zz}^{\text{TM}} j\omega C Z_{\text{Load,eff}}}\right] \tag{2}$$

and

$$M = 2\left(\varepsilon_h - \varepsilon_{zz}^{\text{TM}}\right) + \cosh(\gamma_{\text{TM}}h)\left\{\frac{j\varepsilon_h k_{\text{TEM}}}{\omega C Z_{\text{Load,eff}}}\sin(k_{\text{TEM}}h) + \left[\varepsilon_h\left(\frac{\varepsilon_h}{\varepsilon_{zz}^{\text{TM}}} - 2\right) + 2\varepsilon_{zz}^{\text{TM}}\right]\cos(k_{\text{TEM}}h)\right\} + \left(\varepsilon_h - \varepsilon_{zz}^{\text{TM}}\right)\sinh(\gamma_{\text{TM}}h)\left[\left(\frac{\gamma_{\text{TEM}}}{\gamma_{\text{TM}}} + \frac{\gamma_{\text{TM}}}{\gamma_{\text{TEM}}}\right) \times j\sin(k_{\text{TEM}}h) + \frac{\varepsilon_h\gamma_{\text{TM}}}{\varepsilon_{zz}^{\text{TM}} j\omega C Z_{\text{Load,eff}}}\cos(k_{\text{TEM}}h)\right], \tag{3}$$

where $\gamma_{\text{TM}} = \sqrt{k_p^2 + k_x^2 - k_0^2\varepsilon_h}$ is the complex propagation constant of the TM mode in the uniaxial WM, $\gamma_{\text{TEM}} = jk_{\text{TEM}} = jk_0\sqrt{\varepsilon_h}$ is the propagation factor of the transverse electromagnetic (TEM) mode, $\varepsilon_{zz}^{\text{TM}} = \varepsilon_h k_x^2/(k_p^2 + k_x^2)$ is the relative effective permittivity for TM polarization, $C = 2\pi\varepsilon_h\varepsilon_0/\ln[a^2/4r_0(a - r_0)]$ is the capacitance per unit length of the wire medium as defined in Ref. 29, and $Z_{\text{Load,eff}}$ is the effective load impedance. This impedance includes correction terms due to the parasitic capacitance C_{par} and parasitic inductance L_{par}, due to the nonuniformity in the current and charge distributions in the wire in the presence of a lumped load[18]

$$Z_{\text{Load,eff}} = j\omega L_{\text{par}} + \frac{1}{(j\omega C_{\text{par}} + 1/Z_{\text{Load}})}. \tag{4}$$

Here, Z_{Load} accounts for the type of the lumped load (e.g., inductive or capacitive).

On the other hand, the analytical expression for an odd excitation (PMC symmetry) is such that[30]

$$R_{\text{odd}} = -\frac{\frac{\varepsilon_h k_x^2\tanh(\gamma_{\text{TM}}h)}{\gamma_{\text{TM}}(k_x^2+k_p^2)} + \frac{\varepsilon_h k_p^2\tan(k_{\text{TEM}}h)}{k_{\text{TEM}}(k_x^2+k_p^2)} - \left(\frac{1}{\gamma_0} + j\frac{Y_g\eta_0}{k_0}\right)}{\frac{\varepsilon_h k_x^2\tanh(\gamma_{\text{TM}}h)}{\gamma_{\text{TM}}(k_x^2+k_p^2)} + \frac{\varepsilon_h k_p^2\tan(k_{\text{TEM}}h)}{k_{\text{TEM}}(k_x^2+k_p^2)} + \left(\frac{1}{\gamma_0} - j\frac{Y_g\eta_0}{k_0}\right)} \tag{5}$$

with all the notations defined before.

From the superposition principle, the reflection or transmission coefficients for the bi-layer mushroom structure (see Fig. 1) are given by

$$R = \tfrac{1}{2}(R_{\text{even}} + R_{\text{odd}}), \tag{6}$$

$$T = \tfrac{1}{2}(R_{\text{even}} - R_{\text{odd}}). \tag{7}$$

III. DISPERSION BEHAVIOR OF THE GUIDED MODES

In order to determine the regime in which the charge density waves supported by the metallic grids can be strongly coupled to the radiation field, next we investigate the dispersion behavior of TM^x surface (bound) waves. We restrict our analysis to the case of modes with even symmetry, since the fundamental resonance of the coupled grid system is associated with even modes.

The guided modes dispersion is obtained based on the numerical solution of the dispersion equation [denominator of the reflection coefficient in Eq. (1)] as a root search for the propagation constant k_x. It should be noted that in general the propagation constant k_x is complex valued, however, in this work, we are only interested in the proper real (bound) surface-wave modes, and the leaky waves are not considered here.

The effective medium results for the dispersion behavior of the normalized propagation constant, $\text{Re}(k_x/k_0)$, of the TM^x even guided modes of the bi-layer mushroom structure with different loads are shown in Fig. 2. The structural parameters are as follows: $a = 2$ mm, $g = 0.2$ mm, $r_0 = 0.05$ mm, $\varepsilon_h = 10.2$, and $L = 2$ mm. By comparing the analytical results with full-wave results obtained with HFSS,[32] it is estimated (by curve fitting) that the gap is characterized by the parasitic capacitance $C_{\text{par}} = 0.02$ pF and parasitic inductance $L_{\text{par}} = 0.06$ nH. In the full-wave simulations, the load is inserted in the wires through a gap of 0.1 mm.

Figure 2 reveals several interesting things. First, it is seen that inductive loads lead to a reduction of the resonant

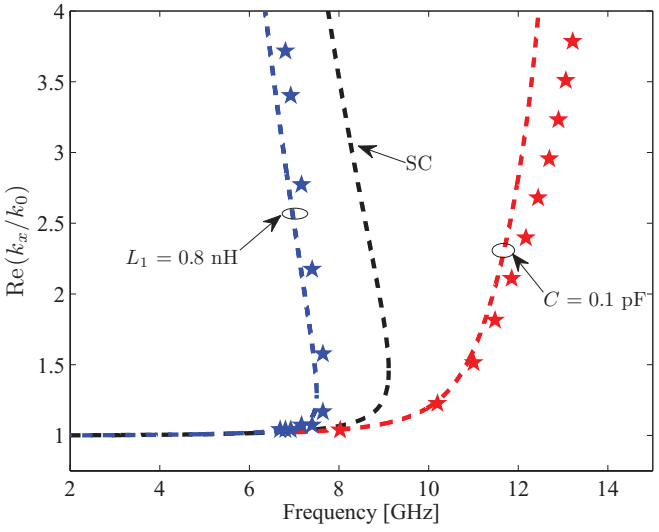

FIG. 2. (Color online) Dispersion behavior of the even guided modes of the bi-layer mushroom structure for the lumped inductive load (0.8 nH), capacitive load (0.1 pF), and a short circuit (SC). The dashed lines represent the homogenization results and the discrete symbols correspond to the full-wave HFSS results.

frequency where the density of guided modes (number of modes per unit of frequency) is maximal and k_x/k_0 is much greater than unity. This occurs because a lumped inductance is combined in series with the distributed inductance of a wire, and hence leads to the increase of the total inductance of the system and to a decrease of the effective plasma frequency.[20] Conversely, a capacitive lumped load behaves effectively as a shunt negative inductive load, and thus contributes to lower the total inductance of the system and to an increase of the resonant frequency.

Typically, the dispersion behavior of the guided modes in case of inductive loads is formed by forward (the phase and group velocities have the same direction) and backward (phase and group velocities have opposite directions) branches, as can be seen in Fig. 2 for two modes with different slopes of the dispersion curves. However, at the frequency of approximately 7.501 GHz, wherein the phase velocities of the forward and backward modes become equal, the propagation stops and the group velocity vanishes. This corresponds to the lower bound of the stopband for the proper real (bound) TM^x guided modes [where $\text{Re}(k_x/k_0) \approx 1.28$]. Even though we consider here only real modes, we prefer to keep the notation of the real part of the normalized propagation constant [$\text{Re}(k_x/k_0)$], such that dielectric and conduction losses can be taken into account.

Ideally, in order to have a strong enhancement of the evanescent waves, we would like the dispersion curve to become maximally flat at the resonant frequency (i.e., to approach a vertical line). In these ideal circumstances, the density of guided modes at the resonant frequency is extremely large, and the free charges in the metallic grids interact resonantly with the radiation field, nearly independent of its spatial variation. However, it can be seen that for the example of Fig. 2 such a dispersion behavior is not obtained with inductive loads, and on the contrary, the inductive loads tend to make the dispersion curve less vertical at the resonant frequency.

On the other hand, the results of Fig. 2 suggest—in particular, the fact that the topology of the dispersion branch changes, such that for a capacitive load the dispersion curve is not folded over itself—that by using capacitive loads it may be possible to tune the dispersion behavior, in such a manner that for some optimal C the dispersion curve may become practically vertical. This can be physically explained as the result of compensation of the inductive mutual coupling of the neighboring mushroom cells by the capacitive interaction of the same cells due to the patch grids. The two mechanisms of coupling have opposite frequency behaviors, therefore by tuning the resonant frequency with the load capacitance one can reach the frequency point where the two effects are balanced. Figure 3 confirms this possibility, and shows that for a capacitive load of 0.2 pF the guided mode dispersion becomes practically flat. Particularly, at 10.69 GHz, the phase velocities of the forward and backward modes become equal, and the propagation of guided modes stops (at the point of vertical slope), which corresponds to the left bound of the stopband for the proper real TM^x modes [where $\text{Re}(k_x/k_0) \approx 2.67$]. Notice that an increase in the value of the capacitive load results in a dispersion curve that approaches the one obtained for the case of short circuit (SC). This observation is also consistent with the reflection phase behavior reported in Ref. 19. In practice, the range of capacitive

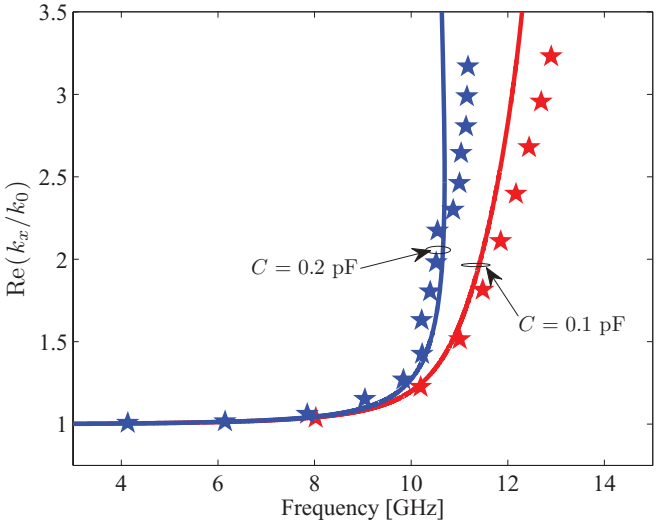

FIG. 3. (Color online) Dispersion behavior of the even guided modes of the bi-layer mushroom structure for capacitive loads of 0.1 and 0.2 pF. The solid lines represent the homogenization results and the symbols correspond to the full-wave HFSS results.

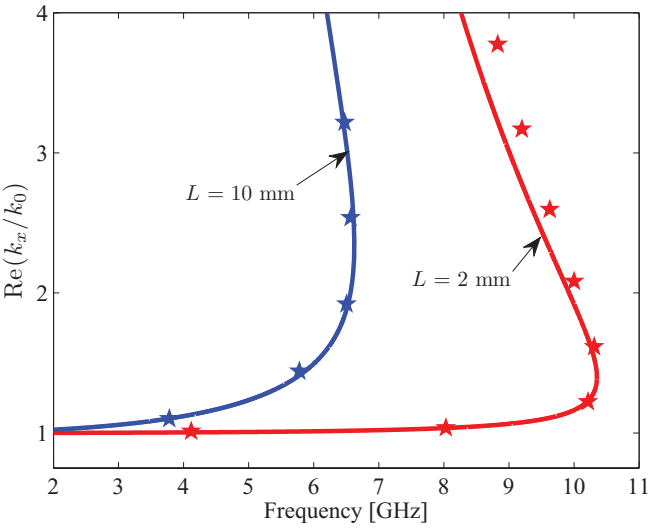

FIG. 4. (Color online) Dispersion behavior of the even guided modes of the bi-layer mushroom structure with inductive loadings of 5 nH for different thicknesses ($L = 2$ and 10 mm) and fixed $a = 2$ mm. The solid lines represent the homogenization results and the symbols correspond to the full-wave HFSS results.

values for which one can achieve significant enhancement of evanescent waves is in between 0.15 and 0.2 pF for the structural parameters considered here. For this range of capacitances, we have always modes such that $k_x a < \pi$ ($k_x a = \pi$ corresponds to the Bragg's condition in the first Brillouin zone). Indeed, the discreteness of the periodic structure limits the range of spatial harmonics for which the effective medium approximation works, and whose amplitude can be boosted by the bi-layer mushroom. To overcome this limitation, we can always further increase the permittivity of the host medium of the metallic wires, but this may not be practical.

Yet, another option to have a strong resonant response with a very compact structure ($a/\lambda \ll 1$ and without using high permittivity substrates) is to increase the length of the metallic wires for a fixed grid period, i.e., to increase L/a. Indeed, the analytical model shows that increasing L/a results in a lower resonant frequency (where the group velocity vanishes), and at the same time in an enhancement of the normalized propagation constant $\mathrm{Re}(k_x/k_0)$. Such an increase in the value of $\mathrm{Re}(k_x/k_0)$ is highly beneficial for the evanescent-wave amplification. Interestingly, for large values of L/a, the optimal load to have a vertical dispersion behavior at low frequencies is an inductive load.

To illustrate this, we consider bi-layer mushroom slab with the following structural parameters: $a = 2$ mm, $g = 0.2$ mm, $r_0 = 0.05$ mm, and $\varepsilon_h = 1$. In Fig. 4, we plot the dispersion behavior of the guided modes of the bi-layer mushroom structure with the inductive load of 5 nH for different thicknesses of the air-filled slab ($L = 2$ and 10 mm). It can be seen that a larger value of L/a leads to a lower value of the resonant frequency (which decreases from 10.35 to 6.62 GHz) and to a dispersion characteristic closer to the ideal one. In particular, at the resonance frequency $\mathrm{Re}(k_x/k_0)$ increases from 1.38 to 2.30. At the same time, our design remains very subwavelength (along the transverse x and y directions) and this guarantees the validity of the effective medium model even for evanescent waves with very short transverse wavelengths. Indeed, the homogenization results are in good agreement with the full-wave HFSS[32] results, shown as symbols in Fig. 4. The effect of the parasitic inductance and the parasitic capacitance is negligible in this example of an air-filled slab. A similar case of the bi-layer mushroom structure with $L = 2$ mm has been presented in Ref. 20, exhibiting a strong negative refraction at an interface with air. However, such a structure is not suitable for subwavelength imaging because the value of $\mathrm{Re}(k_x/k_0)$ corresponding to zero group velocity (as a turning point from forward to backward propagation) is too small, which does not provide amplification of the evanescent waves. On the other hand, with an increase

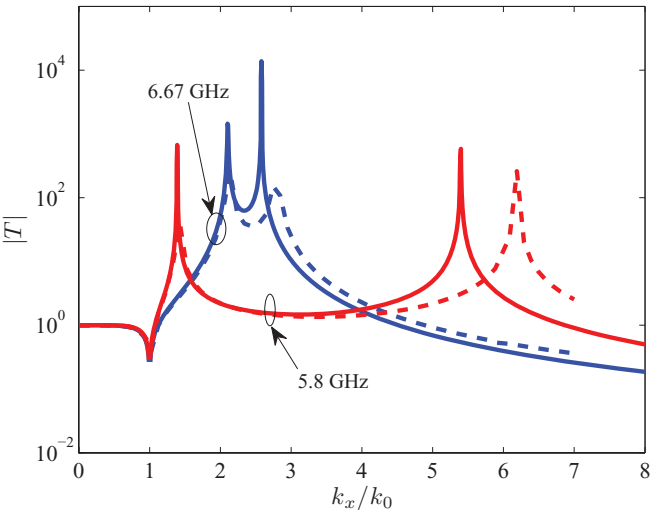

FIG. 5. (Color online) Magnitude of the transmission coefficient $|T|$ as a function of k_x/k_0 calculated for the bi-layer mushroom structure of Fig. 1 with inductive loadings of 5 nH at the center of the vias at the frequencies of 5.8 and 6.67 GHz. The solid lines represent the homogenization results and the dashed lines correspond to the full-wave CST[33] results. The length of the wires in the CST simulations differs by 4% from that of the analytical model.

in the thickness to $L = 10$ mm, the structure does not exhibit a significant negative refraction because the spatial dispersion effects are too strong in the wire medium.

It should be noted that the subwavelength imaging in the silver lens is due to coupling of the plasmons supported by each interface of the lens. Such coupling leads to formation of hybrid plasmonic modes (even and odd modes) of the silver slab. The silver lens operates at a frequency at which both types of modes are excited with about the same amplitude. Rather differently, in our system the two metallic grids are strongly coupled (even if the thickness of the slab is a significantly large fraction of the wavelength), hence, only the even mode is excited in the structure. Indeed, because of the canalization properties of the uniaxial wire medium,[25] the near field of each grid can be effectively channeled by the array of metallic wires, so that the near fields of the two grids can be strongly coupled. Thus our lens operates because of the canalization effect assisted by resonant excitation of the surface waves supported by the patch grids. However, unlike the imaging based on the canalization properties of the uniaxial WM[25] (wherein the image/source planes are distanced from the wire medium by about $a/2$), it will be shown in the next sections that our imaging system may perform well even when the image/source planes are placed at distances significantly larger than the period of the metamaterial, still maintaining the subwavelength resolution.

In the next sections, we investigate the imaging properties of the bi-layer mushroom slab for the cases of inductive and capacitive loading.

IV. IMAGING WITH INDUCTIVE LOADINGS

A. Amplification of evanescent waves

Next, we characterize the transmission characteristics of the propagating and evanescent waves of the bi-layer mushroom structure with inductive loadings and large L/a. We consider the bi-layer mushroom structure (with the geometry shown in Fig. 1) with the following parameters: $\varepsilon_h = 1$, $a = 2$ mm, $g = 0.2$ mm, $L = 10$ mm, $r_0 = 0.05$ mm and with an inductive loading of 5 nH. The predictions of the homogenization model for the transmission magnitude $|T|$ as a function of k_x/k_0, calculated at different frequencies of operation are depicted in Fig. 5. It can be observed that for the case of $|T|$ calculated at the frequency of 6.67 GHz (slightly above the frequency corresponding to the stopband for the proper real modes), $|T|$ is close to unity in the propagating regime $k_x/k_0 < 1$, except in the close vicinity of $k_x/k_0 = 1$. In the evanescent regime where $k_x/k_0 > 1$, $|T|$ greatly exceeds unity, indicating a strong amplification of the near field for the wave vector components in the range $1 < k_x/k_0 < 4$. Such a resonant enhancement due to the presence of the guided (surface-wave) mode can be effectively used to amplify the decaying evanescent fields from the source, leading to a partial recovery of the evanescent field components. On the other hand, at the frequency of 5.8 GHz (see Fig. 5), $|T|$ has two transmission peaks in the evanescent regime at $k_x/k_0 = 1.42$ and 5.27. However, such a behavior is not beneficial for evanescent-wave amplification, because of the lower transmission between the poles, and also due to the narrow range of the wave vector components that are amplified at the poles.

B. Imaging a line source

To characterize the imaging properties of the structure, we consider an infinite magnetic line source directed along the y direction, and placed at a distance d from the upper interface of the structure [with the geometry as shown in Fig. 6(a)]. This 2D infinite magnetic line source is modeled by the current density $\mathbf{J}_m = \hat{\mathbf{y}} I_0 \delta(z - d)\delta(x)$, which produces the incident magnetic

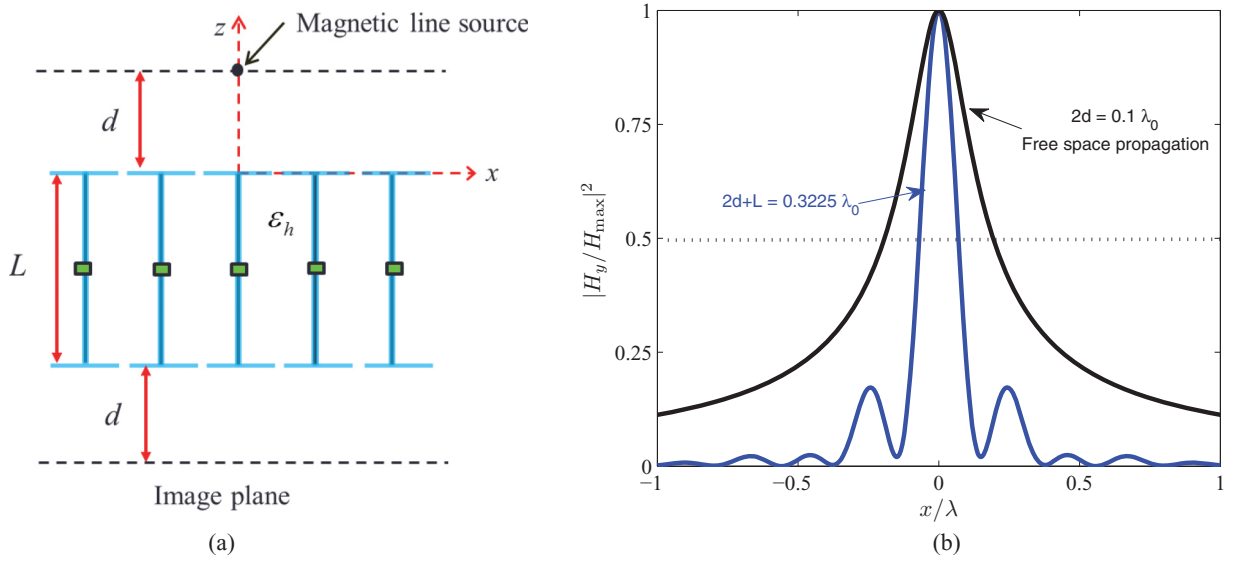

FIG. 6. (Color online) (a) Geometry of the bi-layer mushroom structure with inductively loaded wires excited by a magnetic line source placed at a distance d from the upper interface, with the image plane at a distance d from the lower interface and (b) homogenization results of the square-normalized amplitude of the magnetic field H_y calculated at the image plane. Black curve corresponds to the field profile at the image plane for propagation in free space $2d = 0.1\lambda_0$ (without the structure). Blue curve corresponds to the field profile when the structure is present $2d + L = 0.3225\lambda_0$. The frequency of operation is 6.67 GHz.

field

$$\mathbf{H}(x,z) = \hat{\mathbf{y}} \frac{I_0 k_0^2}{j\omega\mu_0} \left[\frac{1}{4j} H_0^{(2)}(k_0\rho) \right], \quad (8)$$

where $\rho = \sqrt{x^2 + (z-d)^2}$ and $H_0^{(2)}(k_0\rho)$ is the Hankel function of the second kind and order zero. Assuming that the mushroom structure is unbounded in the x and y directions, the magnetic field at a distance d from the lower interface of the structure (image plane) can be expressed by a Sommerfeld-type integral as

$$H_y(x) = \frac{I_0 k_0^2}{j\omega\mu_0\pi} \int_0^\infty \frac{1}{2\gamma_0} e^{-\gamma_0(2d)} T(\omega,k_x) \cos(k_x x) dk_x, \quad (9)$$

where $\gamma_0 = \sqrt{k_x^2 - k_0^2}$ is the propagation constant in free space, and $T(\omega,k_x)$ is the transfer function of the structure given by Eq. (7).

Figure 6(b) shows the square normalized amplitude of the magnetic-field profile calculated at the image plane as a function of x/λ_0 at the operating frequency of 6.67 GHz. It is assumed that $d = 0.05\lambda_0$, and the magnetic line source is in the plane $x = 0$. The results were obtained by numerical integration of the Sommerfeld integral given by Eq. (9) and the structural parameters are the same as in Sec. IV A. The black curve represents the magnetic-field profile for propagation in free space ($2d = 0.1\lambda_0$), and the half-power beamwidth (HPBW) is equal to $0.38\lambda_0$. The field profile at the image plane when the coupled metallic grids are present is depicted by the blue curve. In this case, the distance between the source plane and the image plane is $L + 2d = 0.3225\lambda_0$, and the HPBW is equal to $0.13\lambda_0$, which is four times smaller than the diffraction limited value. For the propagation distance of $L + 2d$ in free space without the structure, the HPBW is $1.14\lambda_0$, thus, showing that the evanescent waves are significantly enhanced by the loaded wire-medium slab. Figure 7(a) shows the calculations of the magnetic-field profile at the image plane for the same structure but with an increase in the distance (d); now $2d = 0.223\lambda_0$. The HPBW when the the coupled metallic grids are present ($L + 2d = 0.445\lambda_0$) is equal to $0.186\lambda_0$. Notice that when the structure is absent the distance is reduced to $2d = 0.223\lambda_0$. For the propagation distance ($2d$) in free space, the HPBW is equal to $0.8\lambda_0$. The resolution of the proposed mushroom lens is $\lambda_0/6$.

In order to confirm the predictions of the homogenization model, the performance of the proposed mushroom-type lens is studied using the commercial electromagnetic simulator HFSS.[32] In HFSS, the magnetic line source is created by considering voltage sources excited in the form of a square loop and considering PMC boundary conditions at the planes $y = 0,a$. The mushroom slab was assumed periodic along the y direction and finite along the x direction. The width of slab was taken to be equal to $W_x \approx 1.8\lambda_0$ along the x direction. The effect of losses is taken into account, and the metallic components are modelled as the copper metal ($\sigma = 5.8 \times 10^7$ S/m). The magnetic-field profiles are calculated at the image plane ($d = 0.11\lambda_0$ from the lower interface of the mushroom structure) along a line parallel to the slab, and are depicted in Fig. 7(a) by dashed lines. It can be observed that there is a remarkable agreement with the homogenization results, despite that the homogenization results refer to an unbounded substrate, whereas the HFSS simulations refer to a finite-width substrate. The results of our simulations (not shown here for brevity) suggest that the width of the slab needs to be relatively large, otherwise we have reflection of surface waves at the edges of the slab which may significantly alter the quality of the imaging. The reason for such a good agreement is that we operate at a very low frequency where the period of the unit cell $a = 0.0445\lambda_0$ is much smaller than the wavelength, and the homogenization results model accurately the physical response of the bi-layer mushroom. In Fig. 7(b), we show the imaging results calculated at the

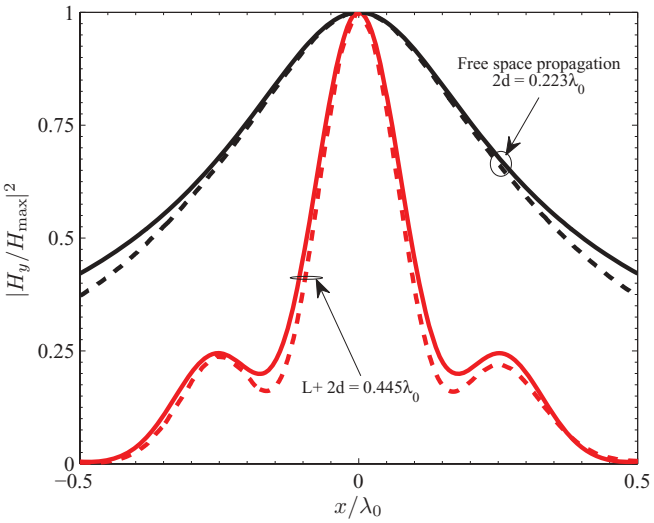

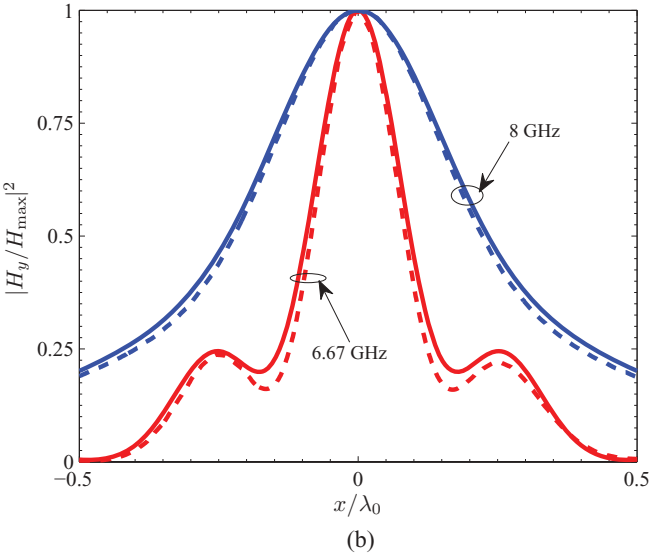

FIG. 7. (Color online) Square-normalized magnitude of the magnetic-field distribution calculated at the image plane for the bi-layer mushroom structure with inductive loadings. (a) Black curves represent the field profile when the structure is absent, and red curves represent the field profile when the structure is present. (b) Magnetic-field profiles calculated at different frequencies when the structure is present; red and blue curves correspond to the operating frequencies of 6.67 and 8 GHz, respectively. The solid lines represent the homogenization results, and the dashed lines correspond to the HFSS results.

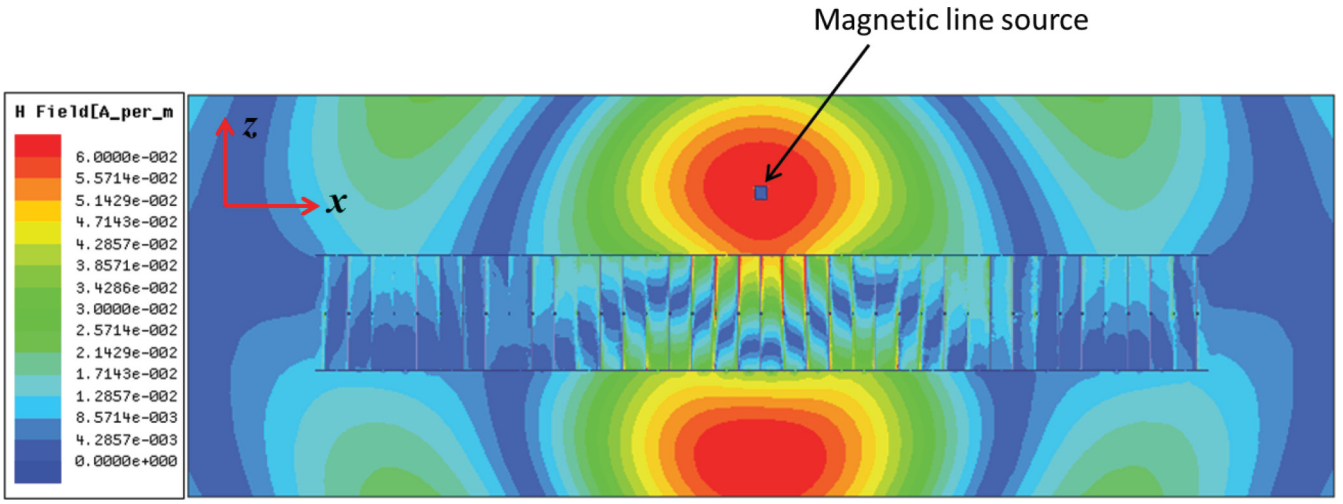

FIG. 8. (Color online) HFSS simulation results showing the snapshot ($t = 0$) of the magnetic-field distribution H_y of the inductively loaded bi-layer mushroom structure. The magnetic line source is placed at a distance $d = 5$ mm from the upper interface, and the image plane is at the same distance d from the lower interface. The width of the slab $W_x = 39a \approx 1.8\lambda_0$ and the frequency of operation is 6.67 GHz.

frequency of 8 GHz; it can be observed that we have an increase in the half-power beamwidth when compared to the case of 6.67 GHz. A snapshot in time of the magnetic field (H_y) at $t = 0$ in the x-z plane calculated using HFSS is shown in Fig. 8, for $f = 6.67$ GHz, and an image at the lower interface of the structure can be observed. The resolution of the image is $\lambda_0/6$ (subwavelength) and is nearly insensitive to the effect of losses which are considered in the numerical simulations.

It should be noted that the evanescent wave amplification can also be achieved for the bi-layer mushroom structure with long wires without inductive loads, i.e., with L/a large. However, the operating frequency is 12% higher when compared to the case of inductive loads and also resolution of image that can be achieved is $\lambda_0/5$ (results are omitted here for sake of brevity). Still, this can be a very interesting option if one wishes to use this structure at terahertz and infrared frequencies where lumped loads are not easily available.

As discussed in Sec. III, another possibility to have superlensing is to consider capacitively loaded short wires (with L/a small) embedded in a high-dielectric constant substrate. In the next section, we characterize the potentials of this solution.

V. IMAGING WITH CAPACITIVE LOADINGS

A. Amplification of evanescent waves

Here, we consider the bi-layer mushroom structure (see Fig. 1) with the following parameters: $\varepsilon_h = 10.2$, $a = 2$ mm, $g = 0.2$ mm, $L = 2$ mm, $r_0 = 0.05$ mm and with a capacitive loading of 0.2 pF. The homogenization and full-wave CST results for the transmission magnitude $|T|$ as a function of k_x/k_0, are depicted in Fig. 9. At the frequency of 10.73 GHz (slightly above the frequency corresponding to the stopband for the proper real modes), a transmission peak (pole) occurs at $k_x/k_0 = 1.77$ (in the evanescent regime where $k_x/k_0 > 1$). Also, in Fig. 9, we plot $|T|$ calculated for the capacitive load of 0.15 pF at the frequency of 11.33 GHz. It can be observed that also in this case, the magnitude of transmission $|T|$ greatly exceeds unity in the evanescent regime, indicating a strong amplifications of the near field. Next, we study the near-field imaging characteristics of the bi-layer mushroom lens.

B. Imaging a line source

We calculated the magnetic-field profile at the image plane for the bi-layer mushroom structure with capacitive loadings of 0.2 pF (the structural parameters are same as those used in the calculations of Fig. 9) by the numerical integration

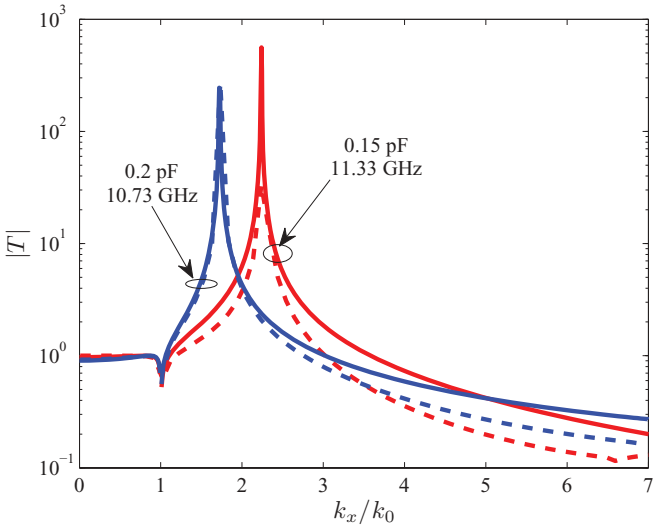

FIG. 9. (Color online) Magnitude of the transmission coefficient $|T|$ as a function of k_x/k_0 calculated for the bi-layer mushroom structure with the capacitive loads of 0.2 pF and 0.15 pF, at the frequencies of 10.73 and 11.33 GHz, respectively. The solid lines represent the homogenization results and the dashed lines correspond to the full-wave CST[33] results. The analytical results are calculated for the capacitive loads of 0.17 and 0.15 pF, at the frequencies of 10.707 and 11.06 GHz, respectively.

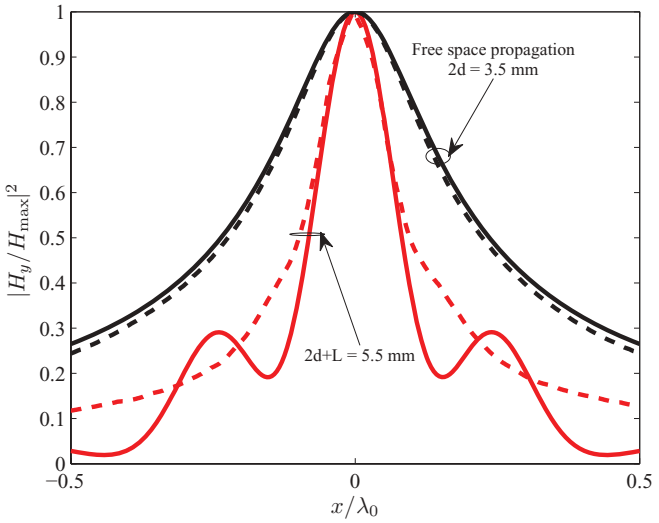

FIG. 10. (Color online) Square-normalized magnitude of the magnetic-field distribution calculated at the image plane for the bi-layer mushroom with capacitive loadings. (a) Black curves represent the field profile for free-space propagation (without the structure), red curves represent the field profile when the structure is present. The solid lines represent the homogenization results calculated at 10.73 GHz, and the dashed lines correspond to the HFSS results calculated at 11.27 GHz.

of Sommerfeld integral given by Eq. (9). The geometry of the problem [see Fig. 6(a)] is the same as in Sec. IV B. It is assumed that the magnetic line source is in the plane $x = 0$ and is placed at a distance, $d = 0.062\lambda_0$, from the upper interface of the lens. Figure 10 shows the square-normalized amplitude of the magnetic-field profile calculated at the image plane as a function of x/λ_0 at the operating frequency of 10.73 GHz. The black curve represents the magnetic-field profile for propagation in free space ($2d = 0.125\lambda_0$), and the HPBW is equal to $0.47\lambda_0$. The field profile at the image plane when the structure is present is depicted by the red curve. Now, the distance between the source plane and the image plane is $L + 2d = 0.196\lambda_0$, and the HPBW is equal to $0.16\lambda_0$, thus, showing that the evanescent waves are significantly enhanced in the capacitively loaded wire-medium slab. In the analytical calculations, the dielectric losses have been taken into account with $\tan\delta = 0.0015$.

Next, we compare the homogenization results with the numerical results using the commercial electromagnetic simulator HFSS.[32] The simulation setup is the same as that outlined in Sec. IV B, except that the width of the slab along the x direction is $W_x = 35a$ and $a = 2$ mm is the period of the unit cell. In HFSS simulations, the effect of losses is taken into account: the metallic components are modeled as copper ($\sigma = 5.8 \times 10^7$ S/m), and a loss tangent of $\tan\delta = 0.0015$ is considered for the dielectric substrate (commercially available RT/duroid 6010LM). The calculated square-normalized magnetic-field profiles at the image plane when the line source is placed at a distance $d = 1.75$ mm from the upper interface of the structure are depicted in Fig. 10, shown as dashed lines. The simulation results predict a superlensing effect at a slightly higher frequency of 11.27 GHz, as compared to the

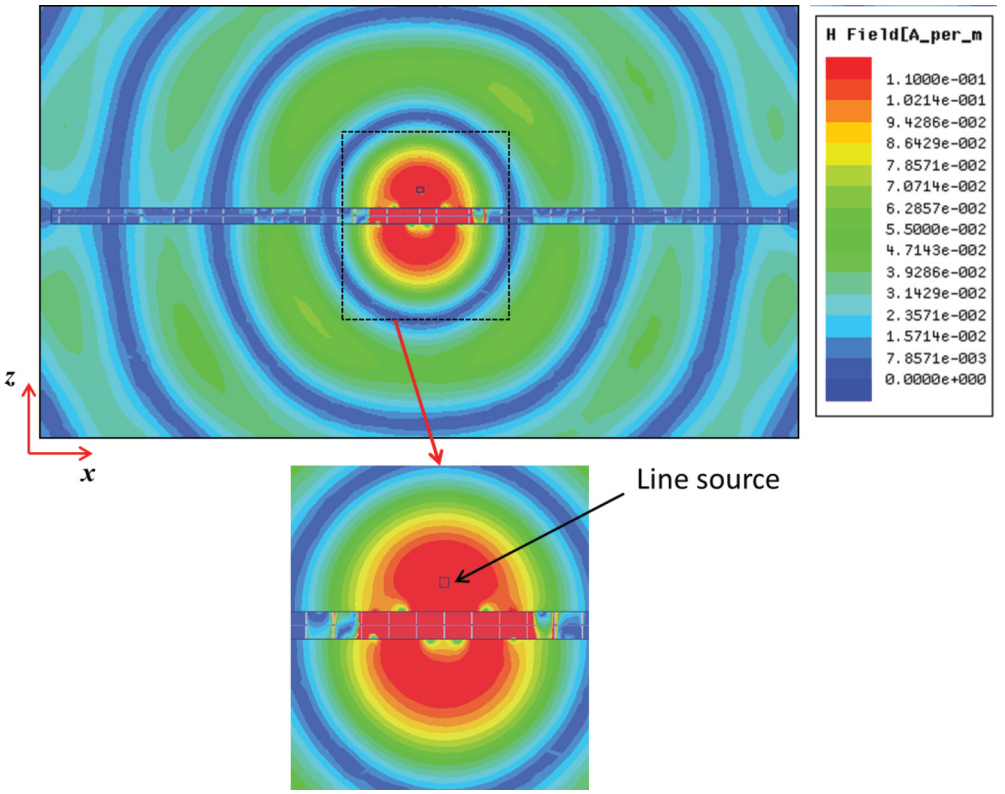

FIG. 11. (Color online) HFSS simulation results showing the snapshot ($t = 0$) of the magnetic-field distribution H_y of the capacitively loaded bi-layer mushroom structure. The magnetic line source is placed at a distance $d = 1.75$ mm from the upper interface, and the image plane is at the same distance d from the lower interface. The width of the slab $W_x = 35a \approx 2.65\lambda_0$, and the frequency of operation is 11.27 GHz.

homogenization results which were obtained at 10.73 GHz. The calculated HPBW at the image plane when the structure is present is $0.19\lambda_0$, which is slightly larger than that predicted using homogenization. Nevertheless, homogenization and simulation results are reasonably consistent and show that the near field can be partially reconstructed by the bi-layer mushroom structure with capacitive loadings. It is important to point out that even though we have a slight quantitative disagreement, the model still captures the pertinent wave phenomena.

A snapshot in time of the magnetic field (H_y) at $t = 0$ in the x-z plane is shown in Fig. 11, at $f = 11.27$ GHz, and the image at the lower interface of the structure can be observed. In spite of the source and the image planes being located at a large distance $2d/L > 1$ when compared to the case of inductive loads (where $2d/L = 1$), the capacitively loaded mushroom lens has a resolution of $\lambda_0/6$. It should be noted that unlike the Pendry's lens,[1] the optimal position of the image/source planes in our system may be different from half the thickness of the structure. Typically, the resolution improves if the image plane is positioned closer to the lens, however the image plane should be sufficiently far away from the lens because otherwise the side lobes caused by the excitation of the surface wave (observed as poles in Figs. 5 and 9) may deteriorate the quality of the image.

VI. CONCLUSION

In this work, we demonstrate the possibility of achieving evanescent-wave enhancement and near-field imaging by using a bi-layer mushroom structure with capacitively/inductively loaded metallic wires. The principle of operation of our system is based on the strong interaction of two metallic grids, coupled by an array of metallic wires. In the case of capacitive loadings, it is possible to obtain a flat dispersion for guided modes by appropriately tuning the capacitive load and a subwavelength design ($a/\lambda \ll 1$) is available with $L \approx a$ based on a high dielectric constant substrate. Another option to have a subwavelength design, which does not require the high-dielectric constant substrate, involves using a structure with long wires ($L/a \gg 1$). The wires can be loaded with lumped inductors in case one wishes to have moderate values of L/a. The proposed designs for sub-wavelength imaging are nearly insensitive to the losses at microwave frequencies, and a resolution of $\lambda_0/6$ has been numerically demonstrated. The analysis has been carried out using the developed nonlocal homogenization models and validated using the full-wave simulations.

ACKNOWLEDGMENTS

S. I. Maslovski acknowledges fruitful discussions with P. A. Belov concerning subwavelength imaging by wire media terminated with metallic patches.

*ckaipa@olemiss.edu

[1] J. B. Pendry, Phys. Rev. Lett. **85**, 03966 (2000).
[2] M. J. Freire and R. Marqués, Appl. Phys. Lett. **86**, 182505 (2005).
[3] Z. Liu, H. Lee, Y. Xiong, C. Sun, and X. Zhang, Science **315**, 1686 (2007).
[4] I. I. Smolyaninov, Y.-J. Hung, and C. C. Davis, Science **315**, 1699 (2007).
[5] R. Merlin, Science **317**, 927 (2007).
[6] A. Grbic and G. V. Eleftheriades, Phys. Rev. Lett. **92**, 117403 (2004).
[7] J. Christensen and F. J. Garcia de Abajo, Phys. Rev. B **82**, 161103 (2010).
[8] T. Taubner, D. Korobkin, Y. Urzhumov, G. Shvets, and R. Hillenbrand, Science **313**, 1595 (2006).
[9] F. Lemoult, G. Lerosey, J. de Rosny, and M. Fink, Phys. Rev. Lett. **104**, 203901 (2010).
[10] J. B. Pendry, Phys. Rev. Lett. **91**, 099701 (2003).
[11] X. S. Rao and C. K. Ong, Phys. Rev. B **68**, 113103 (2003).
[12] S. I. Maslovski, S. A. Tretyakov, and P. Alitalo, J. Appl. Phys. **96**, 1293 (2004).
[13] S. I. Maslovski and S. A. Tretyakov, J. Appl. Phys. **94**, 4241 (2003).
[14] S. I. Maslovski, Opt. Commun. **285**, 3363 (2012).
[15] S. I. Maslovski and S. A. Tretyakov, New J. Phys. **14**, 035007 (2012).
[16] M. G. Silveirinha, C. A. Fernandes, and J. R. Costa, Phys. Rev. B **78**, 195121 (2008).
[17] G. Fedorov, S. I. Maslovski, A. V. Dorofeenko, A. P. Vinogradov, I. A. Ryzhikov, and S. A. Tretyakov, Phys. Rev. B **73**, 035409 (2006).
[18] S. I. Maslovski, T. A. Morgado, M. G. Silveirinha, C. S. R. Kaipa, and A. B. Yakovlev, New J. Phys. **12**, 113047 (2010).
[19] C. S. R. Kaipa, A. B. Yakovlev, S. I. Maslovski, and M. G. Silveirinha, IEEE Antennas Wireless Propagat. Lett. **10**, 1503 (2011).
[20] C. S. R. Kaipa, A. B. Yakovlev, S. I. Maslovski, and M. G. Silveirinha, Phys. Rev. B **84**, 165135 (2011).
[21] A. B. Yakovlev, M. G. Silveirinha, O. Luukkonen, C. R. Simovski, I. S. Nefedov, and S. A. Tretyakov, IEEE Trans. Microwave Theory Tech. **57**, 2700 (2009).
[22] M. J. Lockyear, A. P. Hibbins, and J. R. Sambles, Phys. Rev. Lett. **102**, 073901 (2009).
[23] A. P. Hibbins, B. R. Evans, and J. R. Sambles, Science **308**, 670 (2005).
[24] J. B. Pendry, L. Martin-Moreno, and F. J. Garcia-Vidal, Science **305**, 847 (2004).
[25] P. A. Belov, C. R. Simovski, and P. Ikonen, Phys. Rev. B **71**, 193105 (2005).
[26] Y. Zhao, P. A. Belov, and Y. Hao, J. Opt. A: Pure Appl. Opt. **11**, 075101 (2009).
[27] N. Fang, H. Lee, C. Sun, and X. Zhang, Science **308**, 534 (2005).
[28] P. A. Belov, R. Marques, S. I. Maslovski, I. S. Nefedov, M. Silveirinha, C. R. Simovski, and S. A. Tretyakov, Phys. Rev. B **67**, 113103 (2003).

[29] S. I. Maslovski and M. G. Silveirinha, Phys. Rev. B **80**, 245101 (2009).

[30] A. B. Yakovlev, M. G. Silveirinha, and P. Baccarelli, *Third International Congress on Advanced Electromagnetic Materials in Microwaves and Optics* (London, UK, 2009), p. 348.

[31] O. Luukkonen, C. R. Simovski, G. Granet, G. Goussetis, D. Lioubtchenko, A. V. Raisanen, and S. A. Tretyakov, IEEE Trans. Antennas Propag. **56**, 1624 (2008).

[32] HFSS: High frequency structure simulator based on finite element method, ver. 12.0, Ansoft Corporation http://www.ansoft.com.

[33] CST Microwave Studio 2011, CST GmbH http://www.cst.com.